chemistry

MDPI

Article

Synthesis and Characterization of Quinoxaline-Fused Cyclopenta[*cd*]azulene

Tomohiro Oda [1], Yuina Onishi [1], Akihito Konishi [1,2,*] and Makoto Yasuda [1,2,*]

[1] Department of Applied Chemistry, Graduate School of Engineering, Osaka University, 2-1 Yamadaoka, Suita, Osaka 565-0871, Japan
[2] Innovative Catalysis Science Division, Institute for Open and Transdisciplinary Research Initiatives (ICS-OTRI), Osaka University, Suita, Osaka 565-0871, Japan
* Correspondence: a-koni@chem.eng.osaka-u.ac.jp (A.K.); yasuda@chem.eng.osaka-u.ac.jp (M.Y.); Tel.: +81-6-6879-7384 (A.K. & M.Y.)

Abstract: Azulene-based polycyclic hydrocarbons have garnered much attention as potential materials for organic optoelectronic devices and as molecular models for graphene nanosheets with structural defects. Although various methods for ring fusions to an azulene core have been established for ring fusions to an azulene core, efficient synthetic methodologies for *ortho*- and *peri*-fusion to an azulene core are still lacking, which hinders the investigation of the effect of the *ortho*- and *peri*-fusion on the electronic properties of the embedded azulene core. Herein, we describe the synthesis and characterization of quinoxaline-fused cyclopenta[*cd*]azulene **4** as a new *ortho*- and *peri*-fused azulene derivative. The target molecule **4** was successfully synthesized in four steps from 4-methylazulene. The ring annulation decreased the lowest excitation energy compared with that of azulene and its structural isomer **5** and led to multiple reversible reduction processes. Characterization of the molecular geometry and optoelectronic properties of **4** revealed that the embedded azulene core preserves its original aromaticity, while the fused quinoxaline acts as a nucleophilic and basic site. These features suggest that **4** could serve as a metal ligand, a near-infrared absorber, and a component in organic functional devices.

Keywords: aromaticity; azulene; NIR absorption; redox properties

Academic Editor: Felix Plasser

Received: 8 January 2025
Revised: 21 January 2025
Accepted: 22 January 2025
Published: 23 January 2025

Citation: Oda, T.; Onishi, Y.; Konishi, A.; Yasuda, M. Synthesis and Characterization of Quinoxaline-Fused Cyclopenta[*cd*]azulene. *Chemistry* **2025**, *7*, 15. https://doi.org/10.3390/chemistry7010015

1. Introduction

Azulene ($C_{10}H_8$), a structural isomer of naphthalene, is arguably one of the most intensively investigated nonalternant hydrocarbons. The energy levels of molecular orbitals (MOs) and frontier orbitals of naphthalene and azulene at the simple Hückel molecular orbital model level are shown in Figure 1. For naphthalene, the levels of bonding and antibonding MOs are grouped symmetrically below and above the non-bonding energy α. The highest occupied MO (HOMO) and lowest unoccupied MO (LUMO) coefficients of naphthalene are uniformly distributed with the same magnitude at the same carbon center. For azulene, the symmetry described above concerning occupied and empty orbital energy levels and the matching magnitude of coefficients in frontier orbitals no longer appears. Azulene's HOMO is mainly distributed on the pentagon, but LUMO exists on the heptagon. Its unique bicyclic structure, which can be envisaged as the fusion of a pentagon and a heptagon, endows azulene with remarkable optoelectronic properties, including a large dipole moment (1.08 D) [1], a narrow energy gap between HOMO and LUMO due to their poor spatial overlap [2,3], and an abnormal fluorescence (*anti*-Kasha emission) stemming from the transition from the second excited state to the ground

state [4,5]. These characteristics make azulene a promising candidate for applications in organic electronics [6–9] and bioimaging [10]. Furthermore, recent interest in the defective structures of graphene sheets to modify their structural and/or electronic properties [11–13] has prompted the synthesis and characterization of polycyclic hydrocarbons containing azulene units [14–17].

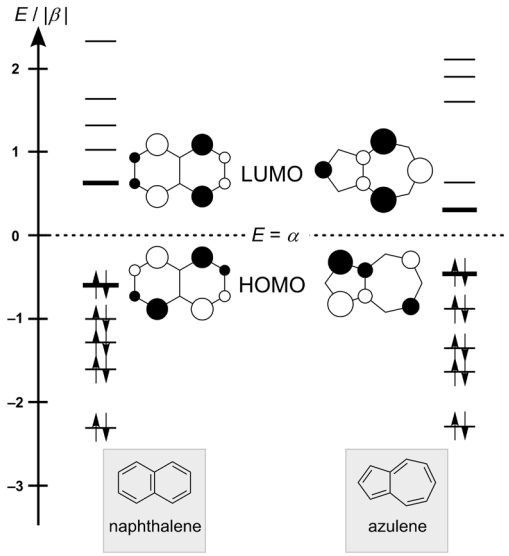

Figure 1. Energy diagrams and frontier orbitals of naphthalene and azulene.

Ring annulation to azulene is an essential strategy for constructing azulene-based polycyclic systems (Figure 2a). Numerous synthetic methods have been established for the *ortho*-fusion of aromatic rings to the pentagon or heptagon of azulene, which has led to a variety of azulenoids and the elucidation of their structure–property relationships. However, the unique electronic properties of the azulene core are often compromised. Even in a planar system, the dominant aromaticity of surrounding benzenoid rings can convert the embedded azulene core into nonaromatic or formally antiaromatic azulene units [18–25]. Another approach for ring annulation is the *ortho*- and *peri*-fusion of π-conjugated units to azulene. However, there is still a lack of efficient synthetic methods for *ortho*- and *peri*-fusion to azulene, which limits the investigation of the effect of *ortho*- and *peri*-annulation on the electronic properties of the embedded azulene core. Nevertheless, recent achievements have demonstrated that benzo-annulation to the *peri*-positions, i.e., the 1,8 or 3,4 positions, of azulene alters its original optoelectronic characteristics and offers additional functionalities such as near-infrared (NIR) absorption by retaining the azulene's orbital distributions [26] and open-shell diradicaloid characteristics by embedding quinoidal characters [27].

In this study, we focused on cyclopenta-annulated azulene derivatives as *ortho*- and *peri*-annulated azulenes (Figure 2b). Cyclopenta[*cd*]azulene **1** [28], the simplest cyclopenta-annulated azulene, was first synthesized by Hafner and co-workers [29,30], who also discovered a unique reactivity involving ring-expansion reactions of **1** with alkynes via 1,4-dipole cycloadditions [31]. Later, Takase found that a Friedel–Crafts-type ring closure of azulene-1,3-dicarboxylate derivatives afforded functionalized cyclopenta[*cd*]azulenes [32]. Studies on the fundamental properties of **1** and its derivatives, including their aromaticity [33–36], bond lengths [37,38], as well as absorption [39] and emission characteristics [40], have demonstrated that the dominant canonical structure of **1** in the ground state is a superposition of aromatic azulene and non- or even antiaromatic pentalene [38]. However, synthetic attempts of π-expansion to the cyclopenta[*cd*]azulene core are rare. So far, only benzo- (**2**) [41] and dibenzo-fused (**3**) [42] derivatives have been reported as the products of the aforementioned 1,4-dipole cycloadditions; however, their physical characteristics

have not been thoroughly investigated. Moreover, other π-extended cyclopenta[*cd*]azulene derivatives have yet to be synthesized. Herein, we describe the design and synthesis of quinoxaline-fused cyclopenta[*cd*]azulene **4**, a structural isomer of π-extended fluoranthene derivative **5** [43], as a new congener of cyclopenta-annulated azulene derivatives (Figure 2c). Quinoxalines are electron-deficient heteroaromatic rings and one of the most common building blocks for *N*-heteroacenes [44–50]. The structure of **4** can be interpreted as a donor (D)–acceptor (A) conjugated system comprising an electron-donating azulene and an electron-withdrawing quinoxaline. As the target molecule **4** had hitherto been unknown, we developed a synthetic strategy for the pentacyclic skeleton. As a result of the cyclopenta-annulated π-expansion of the azulene core, **4** is a planar π-conjugated system that exhibits long-wavelength absorption and the ability to undergo multiple reversible reduction reactions.

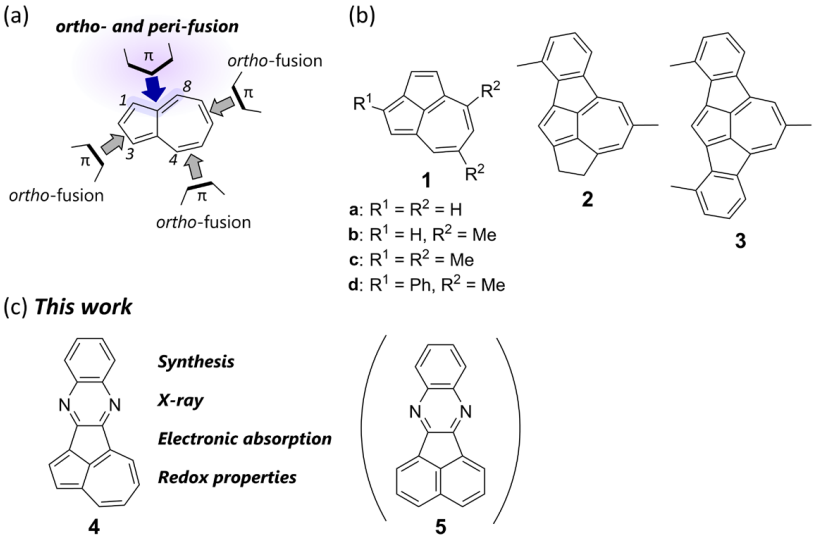

Figure 2. (**a**) Types of ring annulations of π-conjugated units to azulene. (**b**) Molecular structures of cyclopenta-annulated azulene derivatives: cyclopenta[*cd*]azulene **1** and its benzo- (**2**) and dibenzo-fused (**3**) derivatives. (**c**) Targeted quinoxaline-fused cyclopenta[*cd*]azulene **4** and its structural isomer **5**.

2. Materials and Methods

2.1. Chemical Reagents and Instruments

NMR spectra were recorded on a JEOL-ECS400spectrometer (Tokyo, Japan, ^{1}H: 400 MHz; ^{13}C: 100 MHz). The ^{1}H and ^{13}C NMR signals of compounds were assigned using HMQC, HSQC, HMBC, COSY, and ^{13}C off-resonance techniques. Positive FAB, EI, and MALDI-TOF mass spectra were recorded on JEOL JMS-700 (Tokyo, Japan), Shimadzu GCMS-QP2010 Ultra (Kyoto, Japan), and JEOL JMS-S3000 instruments (Tokyo, Japan), respectively. High-resolution DART and ESI mass spectra were measured using a JEOL JMS-T100LP spectrometer (Tokyo, Japan). IR spectra were recorded on a JASCO FT/IR 6200 spectrophotometer (Tokyo, Japan) using thin films or KBr pellets. UV–vis–NIR spectra were recorded on a JASCO V-770 spectrophotometer (Tokyo, Japan). Cyclic voltammetry (CV) measurements were recorded using an ALS-600C electrochemical analyzer (Tokyo, Japan) using a glassy carbon working electrode, a Pt counter electrode, and an $Ag/AgNO_3$ reference electrode at room temperature in THF containing 0.1 M $^{n}Bu_4NClO_4$ as the supporting electrolyte. Data collection for single-crystal X-ray diffraction analyzes was performed on a Rigaku/XtaLAB Synergy-S/Cu diffractometer (Tokyo, Japan, CuKα λ = 1.54187 Å). All nonhydrogen atoms were refined with anisotropic displacement parameters while hydro-

gen atoms were placed at calculated positions and refined riding on their corresponding carbon atoms using the Olex2 program (ver. 1.2) [51].

Anhydrous dichloromethane, THF, acetonitrile, diethyl ether, toluene, hexane, and all other reagents were obtained from common commercial suppliers and used as received. Pristine azulene was purchased from common commercial sources. 4-Methylazulene (**7**) was synthesized from azulene according to reported procedures [52,53]. Compound **5** was synthesized as a reference following a reported method [54]. Details of the synthetic procedures for **4**, **4**$Me^+ \cdot I^-$, **6**, **8**, and **9** are summarized in the Supplementary Materials.

2.2. Compound Characterization

2-(Azulen-4-yl)acetic acid (**8**). Blue solid, mp 122.2 °C–123.0 °C; IR (KBr) ν = 3075 (s), 3009 (s), 2959 (s), 2922 (s), 2638 (m), 2532 (m), 1686 (s), 1562 (s), 1486 (m), 1442 (s), 1393 (s), 1363 (s), 1323 (m), 1267 (s), 1226 (s), 1186 (m), 1070 (w), 1025 (w), 953 (m), 761 (s) cm^{-1}; ^1H NMR (400 MHz, $CDCl_3$) 8.38 (d, *J* = 9.2 Hz, 1H), 7.89 (t, *J* = 4.0 Hz, 1H), 7.59 (t, *J* = 9.6 Hz, 1H), 7.46 (d, *J* = 3.6 Hz, 1H), 7.42 (d, *J* = 4.0, 1H), 7.19 (t, *J* = 9.6 Hz, 1H), 7.19 (d, *J* = 10.4 Hz, 1H), 4.23 (s, 2H); $^{13}C\{^1H\}$ NMR (100 MHz, $CDCl_3$) 176.2, 140.8, 140.5, 137.6, 137.1, 136.7, 136.4, 126.4, 122.8, 119.5, 115.8, 43.3; HRMS (DART$^+$) Calculated ($C_{12}H_{11}O_2$): 187.0754 ([M+H]$^+$), Found: 187.0758.

Cyclopenta[cd]azulen-2(1H)-one (**9**). Purple solid, mp 104.5 °C–105.4 °C; IR (KBr) ν = 3060 (m), 2928 (m), 2293 (w), 1771 (w), 1659 (s), 1589 (s), 1450 (s), 1384 (s), 1327 (s), 1265 (s), 1236 (s), 1202 (s), 1140 (m), 1015 (s), 959 (s), 930 (m), 841 (m), 795 (s), 739 (s) cm^{-1}; ^1H NMR (400 MHz, $CDCl_3$) 8.44 (d, *J* = 9.2 Hz, 1H), 7.95 (d, *J* = 4.4 Hz, 1H), 7.92 (t, *J* = 10.0 Hz, 1H), 7.54 (d, *J* = 4.4 Hz, 1H), 7.53 (dd, *J* = 10.2, 9.8 Hz, 1H), 4.18 (s, 2H); $^{13}C\{^1H\}$ NMR (100 MHz, $CDCl_3$) 192.1, 159.5, 149.3, 139.5, 138.6, 137.8, 131.9, 130.3, 127.2, 123.4, 123.3, 49.8; HRMS (DART$^+$) Calculated ($C_{12}H_9O$): 169.0648 ([M+H]$^+$), Found: 169.0647.

Cyclopenta[cd]azulene-1,2-dione (**6**). Green solid, mp > 300 °C; IR (KBr) ν = 3077 (w), 3036 (w), 2985 (w), 2359 (w), 1871 (w), 1739 (s), 1691 (s), 1605 (s), 1549 (m), 1454 (w), 1436 (w), 1399 (s), 1333 (s), 1297 (m), 1223 (m), 1148 (w), 995 (w), 813 (m), 741 (m) cm^{-1}; ^1H NMR (400 MHz, $CDCl_3$) 8.69 (d, *J* = 10.0 Hz, 1H), 8.45 (d, *J* = 3.6 Hz, 1H), 8.21 (t, *J* = 10.0 Hz, 1H), 7.93 (d, *J* = 9.6 Hz, 1H), 7.82 (d, *J* = 3.6 Hz, 1H), 7.78 (t, *J* = 10.0 Hz, 1H); $^{13}C\{^1H\}$ NMR (100 MHz, $CDCl_3$) 194.8, 177.0, 166.8, 142.4, 139.9, 138.7, 136.9, 132.7, 130.4, 128.9, 124.4, 119.4; HRMS (DART$^+$) Calculated ($C_{12}H_7O_2$): 183.0441 ([M+H]$^+$), Found: 183.0442.

Cyclopenta[3,4]azuleno[1,2-b]quinoxaline (**4**). Green solid, mp 218.1 °C–218.9 °C; IR (KBr) ν = 3090 (w), 3047 (w), 1602 (m), 1563 (s), 1516 (m), 1437 (s), 1335 (m), 1296 (m), 1237 (m), 1081 (m), 981 (w), 795 (s), 764 (s), 742 (s) cm^{-1}; ^1H NMR (400 MHz, $CDCl_3$) 8.62 (d, *J* = 9.2 Hz, 1H), 8.54 (d, *J* = 9.2 Hz, 1H), 8.29 (d, *J* = 4.0 Hz, 1H), 8.28 (dd, *J* = 10.8, 9.6 Hz, 1H), 8.13 (dd, *J* = 8.0, 1.2 Hz, 1H), 8.07 (d, *J* = 8.8, 1.2 Hz, 1H), 7.90 (dd, *J* = 10.8, 9.6 Hz, 1H), 7.72 (ddd, *J* = 8.4, 6.8, 1.6 Hz, 1H), 7.63 (ddd, *J* = 8.4, 7.0, 1.6 Hz, 1H), 7.48 (d, *J* = 4.0 Hz, 1H); $^{13}C\{^1H\}$ NMR (100 MHz, $CDCl_3$) 158.3, 153.0, 147.9, 141.8, 140.9, 139.2, 138.7, 138.3, 136.5, 133.9, 129.9, 129.8, 129.3, 128.7, 127.9, 127.3, 122.6, 120.4; HRMS (DART$^+$) Calculated ($C_{18}H_{11}N_2$): 255.0917 ([M+H]$^+$), Found: 255.0925.

12-Methylcyclopenta[3,4]azuleno[1,2-b]quinoxalin-12-ium iodide (**4**$Me^+ \cdot I^-$). dark brown solid, mp 253.1–254.0 °C; IR (KBr) ν = 3036 (m), 2958 (m), 1943 (w), 1856 (w), 1746 (w), 1671 (w), 1622 (s), 1587 (s), 1534 (m), 1488 (s), 1452 (m), 1419 (s), 1393 (s), 1348 (s), 1251 (m), 1092 (m), 1052 (m), 817 (s), 765 (s) cm^{-1}; ^1H NMR (400 MHz, CD_3CN) 9.16 (d, *J* = 9.6 Hz, 1H), 9.02 (d, *J* = 9.2 Hz, 1H), 8.82 (t, *J* = 10.2 Hz, 1H), 8.59 (t, *J* = 10.2 Hz, 1H), 8.48 (d, *J* = 4.4 Hz, 1H), 8.38 (dd, *J* = 8.2, 1.4 Hz, 1H), 8.21 (dd, *J* = 8.8, 0.8 Hz, 1H), 8.06 (ddd, *J* = 8.8, 7.4 1.4 Hz, 1H), 7.95–7.91 (m, 2H), 4.56 (s, 3H); HRMS (MALDI-TOF MS), Calculated ($C_{19}H_{13}N_2$): 269.1073 ([M−I]$^+$), Found: 269.1044.

3. Results

3.1. Synthesis

The synthetic route to **4** is depicted in Scheme 1. Condensation of 1,2-dicarbonyl and 1,2-diamine compounds is a promising method to obtain the quinoxaline core. For the fusion of the quinoxaline core at the *peri*-position of the azulene core, we revisited the synthesis of cyclopenta[*cd*]azulene-1,2-dione (**6**), which was first synthesized by Hafner in 1974 [30], as a key synthetic precursor. Deprotonation of the methyl group of 4-methylazulene (**7**) with LDA flowed by sparging the reaction mixture with gaseous CO_2 yielded azulene-4-carboxylic acid (**8**) [55]. Following the conditions reported by Hafner [30], **8** underwent a Friedel–Crafts-type cyclization upon treatment with acetic anhydride and pyridine in THF to give cyclic ketone **9**. Oxidation of **9** with selenium dioxide in DMF [56] afforded cyclopenta[*cd*]azulene-1,2-dione (**6**). Finally, the quinoxaline core of **4** was constructed via the condensation of **6** with *o*-phenylenediamine in the presence of LiCl [54] in ethanol, which furnished **4** in 96% yield as a stable dark green solid. *N*-Methylation was then performed by reacting **4** with MeI to give mono *N*-methylated **4**$Me^+ \cdot I^-$. A single-crystal X-ray diffraction analysis revealed that the mono *N*-methylation selectively proceeded at the N(1) atom (See below). This selectivity can be explained by considering the resonance structure shown in Scheme 1 (**4-B**), which shows that the electron donation from the azulene core enhances the nucleophilicity of N(1).

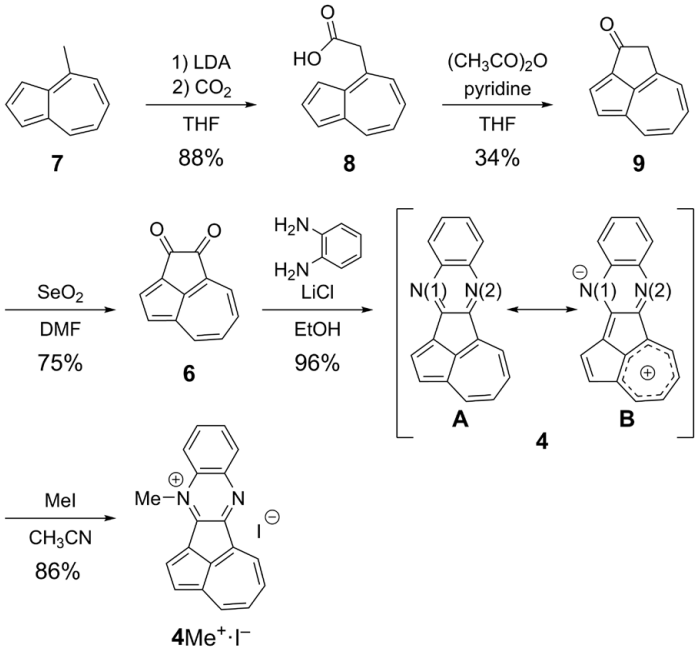

Scheme 1. Synthetic route to **4** and its *N*-methylation to give **4**$Me^+ \cdot I^-$.

3.2. Molecular Geometry of **4**

A single crystal of **4** suitable for an X-ray crystallographic analysis was grown via slow evaporation of a solution of **4** in chloroform and ethyl acetate (Figure 3a). As depicted in Figure 3, the π-surface of **4** adopts an approximate planar geometry. The analysis of the bond lengths (Figure 3b) revealed the electronic structure. Specifically, the C(3)–C(11) (1.452(5) Å) and C(5)–C(12) (1.477(5) Å) bonds, which connect the azulene core and the quinoxaline core, fall within the typical range of the C(sp^2)–C(sp^2) single bond (1.47 Å) and show negligible double-bond character. These features are different from those reported for **1d** [37,38] and reveal that the electronic communication between the two aromatic cores is insignificant. The C(3)–C(11) bond (1.452(5) Å) is shorter than the C(5)–C(12) (1.477(5) Å) bond, illustrating relatively small electronic communication between the azulene core and

the N(1) atom (see the resonance structure of **4** in Scheme 1). The bond-length alternation of the embedded azulene and the quinoxaline core is comparable to those of pristine azulene [57] and 2,3-diphenylquinoxaline [58], respectively. According to these results, the dominant canonical structure of **4** in the ground state can be envisaged as a simple combination of azulene and quinoxaline (such as **4**-**A** in Scheme 1). In the crystal packing, **4** exhibits a slipped 1D π-stacking motif (Figure 3c). Between the adjacent molecules in the slipped 1D column, π–π overlaps mainly involve the cyclopenta[*cd*]azulene and quinoxaline substructures of **4**, separated by an interplanar distance of 3.406 Å. Intermolecular D–A-type interactions between these substructures most likely contribute to the observed packing structure.

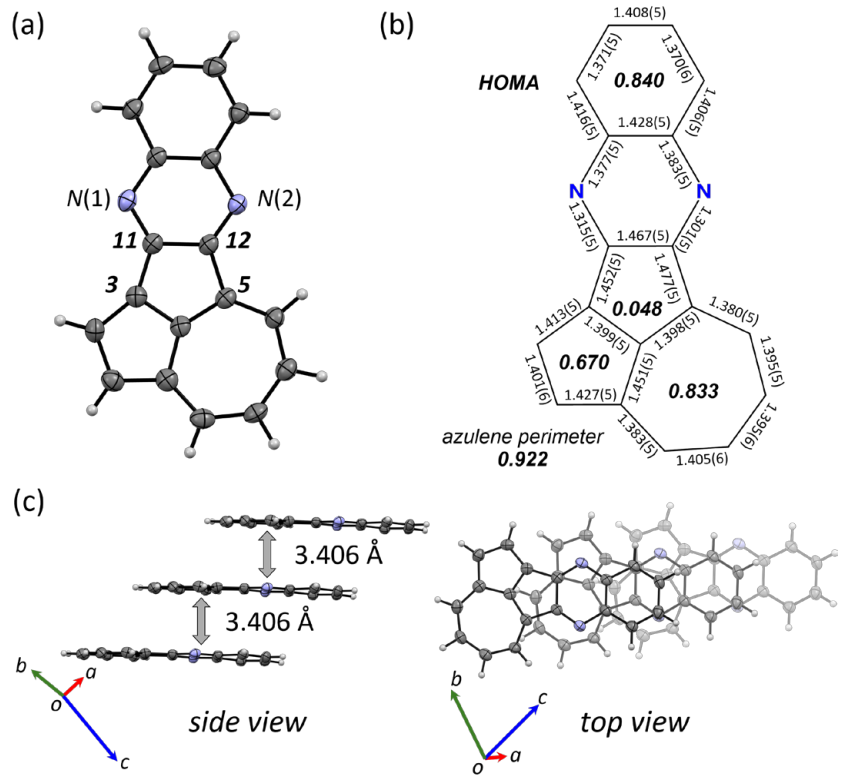

Figure 3. (**a**) Molecular structure of **4** in the crystalline state with thermal ellipsoids at 50% probability. (**b**) Bond lengths and HOMA values (italic) of **4**. (**c**) Side and top views of the packing structure of **4**.

A solution of **4**Me$^+$·I$^-$ in acetonitrile gave a single crystal suitable for an X-ray crystallographic analysis (Figure 4a), which allowed confirming the selective *N*-methylation at the N(1) atom. The HOMO distribution of **4**, which was calculated at the B3LYP/6-311+G*//B3LYP-D3/6-311G* level, explains this selectivity (Figure 5b). In particular, the N(1) atom has HOMO coefficients, whereas the N(2) atom is located at the node of the HOMO. Owing to the injection of a positive charge into **4** via *N*-methylation, the bond lengths of **4**Me$^+$·I$^-$ differ significantly from those of neutral **4** (Figure 4b). In the two pentagons, the C(2)–C(3) bond length increases from 1.413(5) Å for **4** to 1.434(4) Å for **4**Me$^+$·I$^-$, and the C(3)–C(11) bond length decreases from 1.452(5) Å for **4** to 1.414(4) Å for **4**Me$^+$·I$^-$. Simultaneously, the bond-length alternations in the heptagon decreased. The values of the harmonic oscillator model of aromaticity (HOMA) for the heptagon nicely support the structural deformation. The HOMA value of the heptagon of **4**Me$^+$ (0.888) is higher than that of **4** (0.833). These changes in the structure from **4** to **4**Me$^+$ illustrate that the positive charge can be delocalized in a fashion similar to that in a tropylium cation. The *N*-methylated cation **4**Me$^+$ exhibits a slipped π-stacked dimer with a π-to-π distance of 3.347 Å as measured from the distance between the two mean planes (Figure 4c).

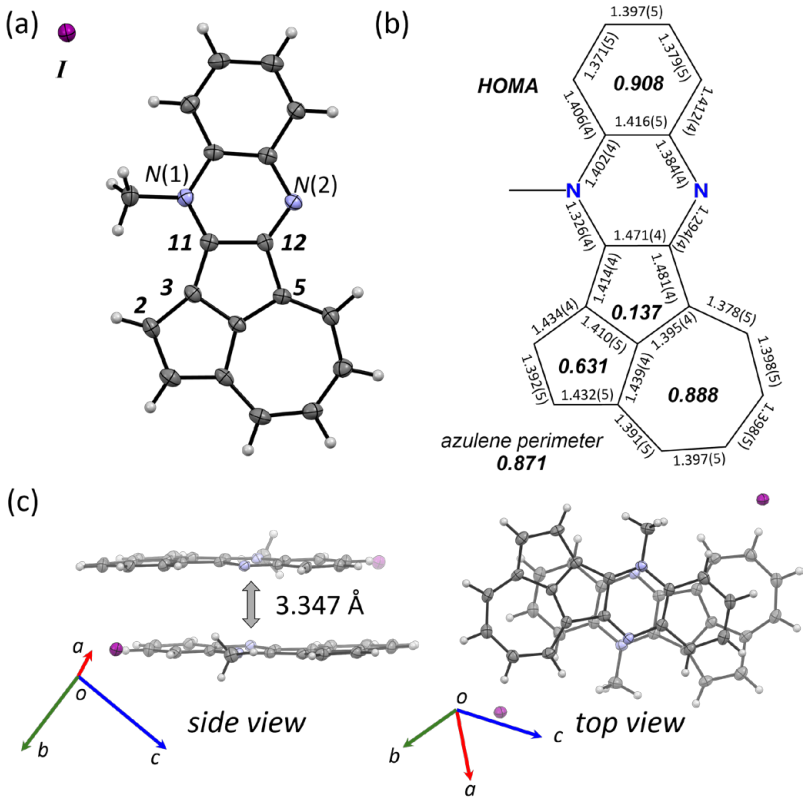

Figure 4. (**a**) Molecular structure of **4**$Me^+ \cdot I^-$ in the crystalline state with thermal ellipsoids at 50% probability. (**b**) Bond lengths and HOMA values (italic) of **4**$Me^+ \cdot I^-$. (**c**) Side and top views of the packing structures of **4**$Me^+ \cdot I^-$.

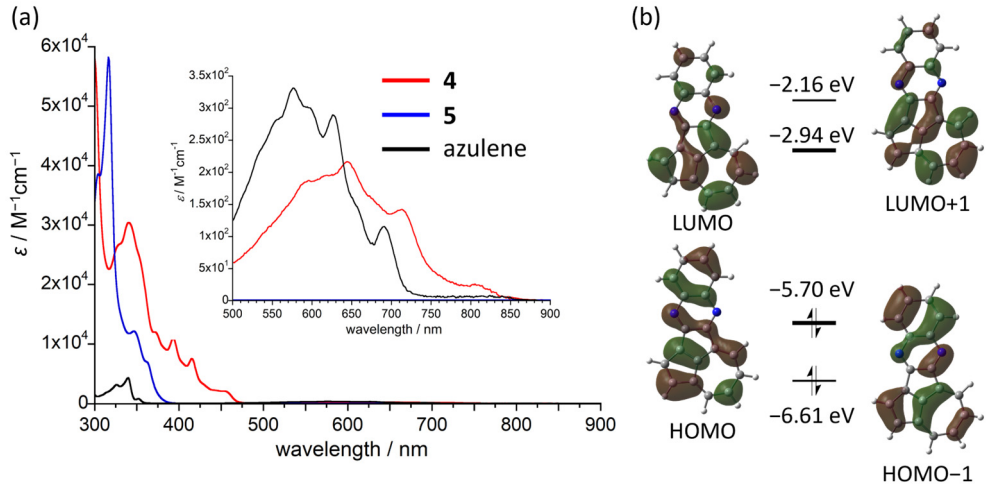

Figure 5. (**a**) Electronic absorption spectra of **4**, **5**, and azulene in THF. (**b**) Frontier molecular orbitals of **4** calculated at the B3LYP/6-311+G*//B3LYP-D3/6-311G* level.

3.3. Optical Properties of **4**

The electronic absorption characteristics of **4** reflect its azulene character. The electronic absorption spectrum of **4** in THF exhibited an intense absorption band from 300 to 450 nm, which was accompanied by weaker absorption bands spanning from 500 to 900 nm (Figure 5a). These weaker absorption bands represent a structured vibrational absorption profile, which is a common feature of the S_0-to-S_1 transition of the azulene moiety [7,59–62]. The longest absorption band (λ_{max} = 851 nm) was shifted to the lower energy region compared to that of azulene (λ_{max} = 691 nm), revealing the π-expansion through the *ortho*- and *peri*-annulation. Notably, the shift of the absorption of **4** to lower energy was more

pronounced than that of the structural isomer **5**. Time-dependent (TD)-DFT calculations at the B3LYP/6-311+G* level ascribed the lowest energy transition for **4** to the HOMO–LUMO transition (638 nm) with a low oscillator strength (f = 0.007), which agrees with the observed results (for details, see Table S1 in the Supporting Information). The HOMO of **4** spreads from the quinoxaline core to the two pentagons, and the LUMO is mainly localized on the cyclopenta[*cd*]azulene substructure (Figure 5b). The spatial overlaps between the HOMO and LUMO are virtually limited to the azulene core, illustrating the similarity of the electronic absorption band of **4** to that of azulene. Furthermore, the spatial difference in the distributions of HOMO and LUMO indicates that the transition has a small charge-transfer contribution. A slight solvatochromism regarding the long-wavelength absorption band was observed for **4** (Figure S3), supporting its charge-transfer nature. In contrast to azulene, no detectable fluorescence was observed even when **4** was excited in the high-energy region (300–500 nm), which can be attributed to the self-absorption in the visible region inhibiting $S_2 \rightarrow S_0$ emissions.

The electronic absorption of the *N*-methylated cation **4**Me$^+$ in $CHCl_3$ revealed an intense absorption band with vibronic progressive features at 479 nm, together with a weak azulene-like band with a structured vibrational profile at ~600–700 nm (Figure 6a). The strong absorbance can be ascribed to the π–π* transition of the *N*-methylated quinoxaline core [63]. The long-wavelength absorption band from the azulene core showed a blue shift compared with that of **4** (Figure S6 and Table S3). TD-DFT calculations at the B3LYP/6-311+G* level reveal that the HOMO–LUMO transition for **4**Me$^+$ (555 nm) can be ascribed to the absorption of the azulene core, which agrees more with the blue-shifted results than that of **4** (Figure S6 and Table S3). The second excited state consists of the HOMO–LUMO+1 transition mainly originating from the cationic quinoxaline core, resulting in an allowed absorption band (431 nm, f = 0.1271). The effect of the protonation on **4** was also investigated via UV–vis spectroscopy (Figure 6b). Compound **4** was protonated by successive additions of trifluoroacetic acid (TFA). Upon exposure to TFA, a new peak with vibronic progressive features was observed at 475 nm, and the lowest energy absorption at around 550 nm from the azulene core exhibited a blue shift compared with that of **4**. The absorption spectrum obtained after adding an excess of TFA (50 eq.) was almost identical to that of the *N*-methylated cation **4**Me$^+$, indicating that monoprotonation occurred on the most basic nitrogen atom rather than on the azulene core. The ^{1}H NMR spectra of **4** in the presence of TFA displayed ten proton signals in the aromatic region, which agrees with an *N*-protonation rather than the generation of an azulenium cation. Moreover, the protonation was reversible, since the initial absorption spectrum of **4** was recovered upon addition of Et_3N (Scheme 2). Trifluoromethanesulfonic acid (TfOH), which is a stronger acid than TFA, was ineffective at giving a doubly protonated compound.

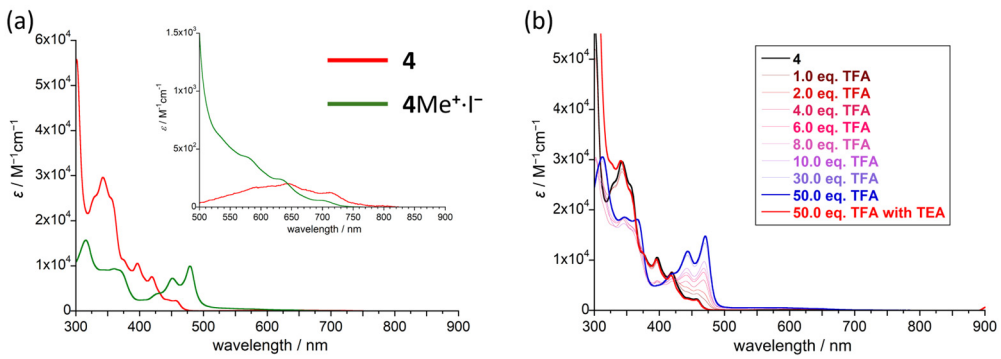

Figure 6. (**a**) Electronic absorption spectra of **4** and **4**Me$^+$·I$^-$ in $CHCl_3$. (**b**) Variable electronic absorption spectra of **4** upon titration with TFA in $CHCl_3$ (TEA = Et_3N).

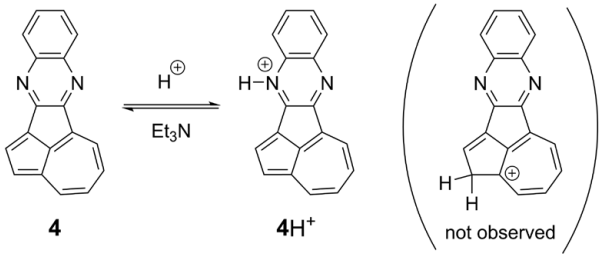

Scheme 2. Protonation of **4** and deprotonation of **4**H$^+$.

3.4. Redox Behavior of **4**

The redox properties of **4** were examined via CV and differential pulse voltammetry (DPV) measurements (Figure 7). The CV curve of **4** in THF exhibits two reversible reduction waves and two irreversible oxidation waves. Using DPV measurements, the redox potentials of **4** were determined to be $E_2^{ox,\,pa}$ = +0.95 V, $E_1^{ox,\,pa}$ = +0.71 V, E_1^{red} = −1.53 V, and E_2^{red} = −2.35 V vs. Fc/Fc$^+$ in THF. Two steps of single-electron processes would give radical anion/cation (**4**$^{\bullet+}$/**4**$^{\bullet-}$) and dianion/dication species (**4**$^{2+}$/**4**$^{2-}$). In the reduced state of **4**, a 6π-aromatic cyclopentadienyl anion substructure appears, which would explain the highly reversible reduction processes in the CV curve. The *N*-methylated cation **4**Me$^+$ gave two reversible reduction waves with more positive potentials compared with those of **4** due to the presence of a positive charge (E_1^{red} = −0.87 V and E_2^{red} = −1.55 V vs. Fc/Fc$^+$ in acetonitrile; Figure S4).

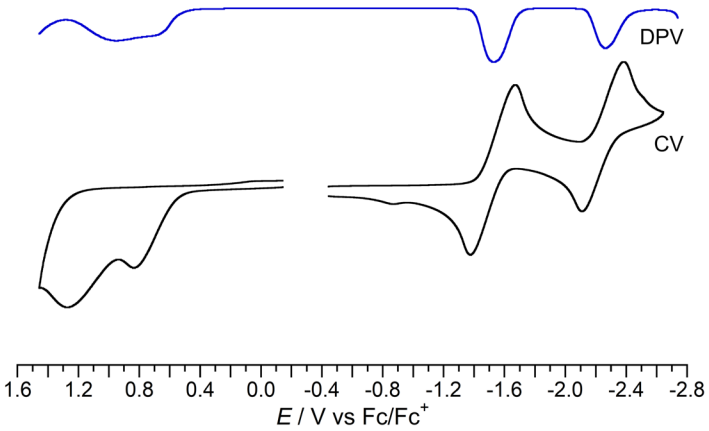

Figure 7. Cyclic voltammogram and differential pulse voltammogram of **4** (V vs. Fc/Fc$^+$; in 0.1 M *n*Bu$_4$NClO$_4$/THF; scan rate = 100 mV/s; room temperature).

4. Discussion

The magnetic criteria for aromaticity illustrate the π-conjugation characteristics of **4** (Figure 8a,b). NICS(1) calculations revealed that the azulene and quinoxaline moieties of **4** show negative values (−10.1 and −9.93 ppm for azulene and −6.60 and −9.88 ppm for quinoxaline), indicating the retention of their original aromatic nature. Meanwhile, the internal pentagon behaves as a nonaromatic ring (–0.18 ppm), supporting that the pentagon works as a simple junction between the two aromatic substructures. According to the anisotropy of the induced current density (ACID) [64,65] calculations on **4**, the induced clockwise ring currents independently flow on the azulene and quinoxaline moieties. The electrostatic potential (ESP) map of **4** revealed D–A characteristics, according to which the quinoxaline moiety carries a partial negative charge and the azulene core a partial positive charge.

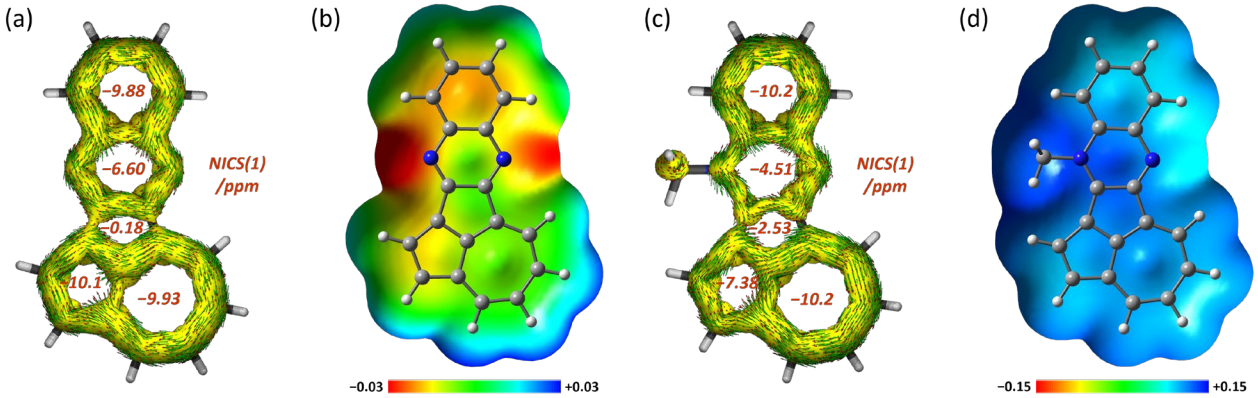

Figure 8. (**a**) ACID plots with NICS(1) values of **4** calculated at the CSGT or GIAO-B3LYP/6-311+G* level. (**b**) ESP map of **4** calculated at the B3LYP/6-311+G* level. (**c**) ACID plots with NICS(1) values of **4**Me$^+$ calculated at the CSGT or GIAO-B3LYP/6-311+G* level. (**d**) ESP map of **4**Me$^+$ calculated at the B3LYP/6-311+G* level.

For *N*-methylated **4**Me$^+$, the heptagon in the azulene moiety exhibits a more negative NICS value (−10.2 ppm) than that of **4**, showing tropylium character (Figure 8c). The ESP map of **4**Me$^+$ indicates some delocalization of the positive charge from the N(1) atom to the heptagon (Figure 8d). However, according to the ACID plot of **4**Me$^+$, the electronic interactions between the azulene and quinoxaline moieties remain small.

5. Conclusions

We synthesized and characterized quinoxaline-fused cyclopenta[*cd*]azulene **4** as an isomer of **5**. The cyclopenta-fusion at the *peri*-position of the azulene core identifies **4** as a new congener of cyclopenta-annulated azulenes with D–A characteristics. Compound **4** displayed a redshift of its longest absorption band and reversible multistage reduction processes. The azulene core of **4** retained its original aromatic character. Moreover, the fused quinoxaline serves as a nucleophilic and basic site. Further studies on the application of **4** as a ligand to coordinate metal centers and as a component of organic functional devices, as well as on its reactivity, will enhance our understanding of the electronic effects of the cyclopenta-annulation on the azulene core.

Supplementary Materials: The following supporting information can be downloaded at: https://www.mdpi.com/article/10.3390/chemistry7010015/s1, Figure S1: Molecular structure of **4** in the crystalline state measured at 123 K; Figure S2: Molecular structure of **4**Me$^+$·I$^-$ in the crystalline state measured at 123 K; Figure S3: (a) Electronic absorption spectra of **4** and **4**Me$^+$·I$^-$ in $CHCl_3$; (b) Expanded electronic absorption spectra of **4** in various solvents; Figure S4: Cyclic voltammogram of **4**Me$^+$·I$^-$; Figure S5: Calculated orbital energy diagram of the HOMO–1, HOMO, LUMO, and LUMO+1 for **4** and **5**; Figure S6: Calculated orbital energy diagram of the HOMO–1, HOMO, LUMO, and LUMO+1 for **4**Me$^+$; Tables S1–S3: Excitation energies of **4**, **5**, and **4**Me$^+$; Tables S4–S6: Optimized geometries for **4**, **5**, and **4**Me. References [51–54,65,66] are cited in the Supplementary Materials.

Author Contributions: Conceptualization, A.K.; investigation, T.O., Y.O. and A.K.; writing—original draft preparation, T.O., Y.O. and A.K.; writing—review and editing, A.K. and M.Y.; supervision, A.K. and M.Y.; project administration, A.K. and M.Y.; funding acquisition, A.K. and M.Y. All authors have read and agreed to the published version of the manuscript.

Funding: This research was funded by JSPS KAKENHI grants JP23K17845 (to M.Y.) and JP23K26643 (to A.K.) by a MEXT Grants-in-Aid for Transformative Research Areas (A) "Digitalization-driven Transformative Organic Synthesis (Digi-TOS)" (JP21H05212 (to M.Y.)) and "Condensed Conjugation" (JP23H04028 (to A.K.)), as well as by JST CREST grant JPMJCR20R3 (Japan).

Data Availability Statement: The original contributions presented in the study are included in the article/Supplementary Materials, and further inquiries can be directed to the corresponding author/s.

Acknowledgments: We thank N. Kanehisa (Osaka Univ.) for valuable advice regarding X-ray crystallography. We acknowledge the Analytical Instrumentation Facility, Graduate School of Engineering, Osaka University (Japan).

Conflicts of Interest: The authors declare no conflicts of interest.

References

1. Anderson, A.G.; Steckler, B.M. Azulene. VIII. A Study of the Visible Absorption Spectra and Dipole Moments of Some 1- and 1,3-Substituted Azulenes[1,2]. *J. Am. Chem. Soc.* **1959**, *81*, 4941–4946. [CrossRef]
2. Michl, J.; Thulstrup, E.W. Why Is Azulene Blue and Anthracene White? A Simple Mo Picture. *Tetrahedron* **1976**, *32*, 205–209. [CrossRef]
3. Gleiter, R.; Haberhauer, G.; Hoffmann, R. *Aromaticity and Other Conjugation Effects*; Wiley-VCH: Weinheim, Germany, 2012; ISBN 978-3-527-32934-2.
4. Beer, M.; Longuet-Higgins, H.C. Anomalous Light Emission of Azulene. *J. Chem. Phys.* **1955**, *23*, 1390–1391. [CrossRef]
5. Dunlop, D.; Ludvíková, L.; Banerjee, A.; Ottosson, H.; Slanina, T. Excited-State (Anti)Aromaticity Explains Why Azulene Disobeys Kasha's Rule. *J. Am. Chem. Soc.* **2023**, *145*, 21569–21575. [CrossRef]
6. Xin, H.; Gao, X. Application of Azulene in Constructing Organic Optoelectronic Materials: New Tricks for an Old Dog. *Chempluschem* **2017**, *82*, 945–956. [CrossRef] [PubMed]
7. Xin, H.; Hou, B.; Gao, X. Azulene-Based π-Functional Materials: Design, Synthesis, and Applications. *Acc. Chem. Res.* **2021**, *54*, 1737–1753. [CrossRef]
8. Zeng, H.N.; Png, Z.M.; Xu, J. Azulene in Polymers and Their Properties. *Chem. Asian J.* **2020**, *15*, 1904–1915. [CrossRef] [PubMed]
9. Huang, J.; Huang, S.; Zhao, Y.; Feng, B.; Jiang, K.; Sun, S.; Ke, C.; Kymakis, E.; Zhuang, X. Azulene-Based Molecules, Polymers, and Frameworks for Optoelectronic and Energy Applications. *Small Methods* **2020**, *4*, 2000628. [CrossRef]
10. Murfin, L.C.; Lewis, S.E. Azulene—A Bright Core for Sensing and Imaging. *Molecules* **2021**, *26*, 353. [CrossRef]
11. Thiemann, F.L.; Rowe, P.; Zen, A.; Müller, E.A.; Michaelides, A. Defect-Dependent Corrugation in Graphene. *Nano Lett.* **2021**, *21*, 8143–8150. [CrossRef]
12. Fei, Y.; Liu, J. Synthesis of Defective Nanographenes Containing Joined Pentagons and Heptagons. *Adv. Sci.* **2022**, *9*, 2201000. [CrossRef] [PubMed]
13. Wu, B.; Meng, H.; Chen, X.; Guo, Y.; Jiang, L.; Shi, X.; Zhu, J.; Long, J.; Gao, W.; Zeng, F.; et al. Structural Modulation of Nanographenes Enabled by Defects, Size and Doping for Oxygen Reduction Reaction. *Angew. Chem. Int. Ed.* **2024**, *64*, e202415071. [CrossRef]
14. Razus, A.C. Syntheses of Azulene Embedded Polycyclic Compounds. *Symmetry* **2024**, *16*, 382. [CrossRef]
15. Konishi, A.; Yasuda, M. Breathing New Life into Nonalternant Hydrocarbon Chemistry: Syntheses and Properties of Polycyclic Hydrocarbons Containing Azulene, Pentalene, and Heptalene Frameworks. *Chem. Lett.* **2021**, *50*, 195–212. [CrossRef]
16. Chaolumen; Stepek, I.A.; Yamada, K.E.; Ito, H.; Itami, K. Construction of Heptagon-Containing Molecular Nanocarbons. *Angew. Chem. Int. Ed.* **2021**, *60*, 23508–23532. [CrossRef]
17. Konishi, A.; Horii, K.; Yasuda, M. The Road to Bis-Periazulene (Cyclohepta[*Def*]Fluorene): Realizing One of the Long-Standing Dreams in Nonalternant Hydrocarbons. *J. Phys. Org. Chem.* **2023**, *36*, e4495. [CrossRef]
18. Konishi, A.; Morinaga, A.; Yasuda, M. Construction of Polycyclic π-Conjugated Systems Incorporating an Azulene Unit Following the Oxidation of 1,8-Diphenyl-9,10-Bis(Phenylethynyl)Phenanthrene. *Chem. Eur. J.* **2018**, *24*, 8548–8552. [CrossRef]
19. Sasaki, Y.; Takase, M.; Okujima, T.; Mori, S.; Uno, H. Synthesis and Redox Properties of Pyrrole- and Azulene-Fused Azacoronene. *Org. Lett.* **2019**, *21*, 1900–1903. [CrossRef]
20. Zhang, X.; Huang, Y.; Zhang, J.; Meng, W.; Peng, Q.; Kong, R.; Xiao, Z.; Liu, J.; Huang, M.; Yi, Y.; et al. Dicyclohepta[*Ijkl*,*Uvwx*]Rubicene with Two Pentagons and Two Heptagons as a Stable and Planar Non-benzenoid Nanographene. *Angew. Chem. Int. Ed.* **2020**, *59*, 3529–3533. [CrossRef] [PubMed]
21. Wang, S.; Tang, M.; Wu, L.; Bian, L.; Jiang, L.; Liu, J.; Tang, Z.-B.; Liang, Y.; Liu, Z. Linear Nonalternant Isomers of Acenes Fusing Multiple Azulene Units. *Angew. Chem. Int. Ed.* **2022**, *61*, e202205658. [CrossRef]
22. Duan, C.; Zhang, J.; Xiang, J.; Yang, X.; Gao, X. Azulene-Embedded [*n*]Helicenes (*n* = 5, 6 and 7). *Angew. Chem. Int. Ed.* **2022**, *61*, e202201494. [CrossRef] [PubMed]
23. Ong, A.; Tao, T.; Jiang, Q.; Han, Y.; Ou, Y.; Huang, K.; Chi, C. Azulene-Fused Acenes. *Angew. Chem. Int. Ed.* **2022**, *61*, e202209286. [CrossRef]
24. Liang, Y.; Wang, S.; Tang, M.; Wu, L.; Bian, L.; Jiang, L.; Tang, Z.-B.; Liu, J.; Guan, A.; Liu, Z. Cascade Synthesis of Benzotriazulene with Three Embedded Azulene Units and Large Stokes Shifts. *Angew. Chem. Int. Ed.* **2023**, *62*, e202218839. [CrossRef]

25. Liu, R.; Fu, Y.; Wu, F.; Liu, F.; Zhang, J.-J.; Yang, L.; Popov, A.A.; Ma, J.; Feng, X. Modular Synthesis of Structurally Diverse Azulene-Embedded Polycyclic Aromatic Hydrocarbons by Knoevenagel-Type Condensation. *Angew. Chem. Int. Ed.* **2023**, *62*, e202219091. [CrossRef]
26. Pigulski, B.; Shoyama, K.; Würthner, F. NIR-Absorbing ΠI-Extended Azulene: Non-Alternant Isomer of Terrylene Bisimide. *Angew. Chem. Int. Ed.* **2020**, *59*, 15908–15912. [CrossRef] [PubMed]
27. Horii, K.; Kishi, R.; Nakano, M.; Shiomi, D.; Sato, K.; Takui, T.; Konishi, A.; Yasuda, M. Bis-Periazulene (Cyclohepta[*def*]Fluorene) as a Nonalternant Isomer of Pyrene: Synthesis and Characterization of Its Triaryl Derivatives. *J. Am. Chem. Soc.* **2022**, *144*, 3370–3375. [CrossRef] [PubMed]
28. Hafner, K.; Schneider, J. Darstellung Und Eigenschaften von Derivaten Des Pentalens Und Heptalens. *Justus Liebigs Ann. Chem.* **1959**, *624*, 37–47. [CrossRef]
29. Hafner, K.; Bangert, K.; Zur Kenntnis Der Azulene, X. Über Azulen-enamine Und Deren Umwandlung in Tricyclische Pentalen- Und Heptalen-Derivate. *Justus Liebigs Ann. Chem.* **1961**, *650*, 98–115. [CrossRef]
30. Hafner, K.; Meinhardt, K.-P.; Richarz, W. Cyclopent[Cd]Azulene and 1,2-Dihydrodicyclopent-[Cd,Ij]Azulene. *Angew. Chem. Int. Ed. Engl.* **1974**, *13*, 204–205. [CrossRef]
31. Diehl, H.; Hafner, K. 1,4-Dipolar Cycloadditions of Cyclopent[Cd]Azulene. *Angew. Chem. Int. Ed. Engl.* **1976**, *15*, 107–108. [CrossRef]
32. Nakadate, T.; Morita, T.; Takase, K. The Formation of Cyclopent[Cd]Azulene and Benz[Cd]Azulene Derivatives by a Friedel–Crafts-Type Ring Closure of Diethyl 4-Phenylethynyl- and diethyl 4-styrylazulene-1,3-dicarboxylates with Polyphosphoric Acid. *Chem. Lett.* **1977**, *6*, 591–594. [CrossRef]
33. Chatterjee, H.; Ali, M.A. Application of Refined MO Method to Hafner's Hydrocarbons. *Tetrahedron* **1964**, *20*, 2829–2834. [CrossRef]
34. DasGupta, N.K.; Ali, M.A. S.C.F.M.O. Study of Hafner's Hydrocarbons. *Theor. Chim. Acta* **1966**, *4*, 101–107. [CrossRef]
35. Dasgupta, A.; Dasgupta, N.K. Aromaticity of Some Nonbenzenoid and Semibenzenoid Hydrocarbons. *Tetrahedron* **1972**, *28*, 3587–3601. [CrossRef]
36. Zhou, Z.; Parr, R.G. New Measures of Aromaticity: Absolute Hardness and Relative Hardness. *J. Am. Chem. Soc.* **1989**, *111*, 7371–7379. [CrossRef]
37. Lindner, H.J. Crystal and Molecular Structure of 5,7-Dimethyl-2-Phenylcyclopent[Cd]-Azulene. *J. Chem. Soc. B Phys. Org.* **1970**, *3794*, 907. [CrossRef]
38. Hafner, K. Structure and Reactivity of Polycyclic Cross-Conjugated π-Electron Systems. *Pure Appl. Chem.* **1971**, *28*, 153–180. [CrossRef]
39. Yamaguchi, H.; Terasaka, T.; Nakajima, T. Electronic Spectra of Hafner's Hydrocarbons. *Theor. Chim. Acta* **1970**, *18*, 255–257. [CrossRef]
40. Dhingra, R.C.; Poole, J.A. Anomalous Emission from Substituted Hafner's Hydrocarbons. *J. Chem. Phys.* **1968**, *48*, 4829–4832. [CrossRef]
41. Hafner, K.; Diehl, H.; Richarz, W. Cycloadditions of Aceheptylene? A Facile Synthesis of Dicyclopenta[Ef,Kl]Heptalenes. *Angew. Chem. Int. Ed. Engl.* **1976**, *15*, 108–109. [CrossRef]
42. Hafner, K.; Diesel, H.D.; Richarz, W. Synthesis of Penta- and Hexacyclic Conjugated Hydrocarbons by Cycloaddition Reactions. *Angew. Chem. Int. Ed. Engl.* **1978**, *17*, 763–764. [CrossRef]
43. Yadav, J.; Reddy, B.; Premalatha, K.; Shiva Shankar, K. Bismuth(III)-Catalyzed Rapid Synthesis of 2,3-Disubstituted Quinoxalines in Water. *Synthesis* **2008**, *2008*, 3787–3792. [CrossRef]
44. Richards, G.J.; Hill, J.P.; Mori, T.; Ariga, K. Putting the 'N' in ACENE: Pyrazinacenes and Their Structural Relatives. *Org. Biomol. Chem.* **2011**, *9*, 5005. [CrossRef]
45. Bunz, U.H.F.; Engelhart, J.U.; Lindner, B.D.; Schaffroth, M. Large N-Heteroacenes: New Tricks for Very Old Dogs? *Angew. Chem. Int. Ed.* **2013**, *52*, 3810–3821. [CrossRef]
46. Bunz, U.H.F. The Larger Linear N-Heteroacenes. *Acc. Chem. Res.* **2015**, *48*, 1676–1686. [CrossRef]
47. Bunz, U.H.F.; Freudenberg, J. N-Heteroacenes and N-Heteroarenes as N-Nanocarbon Segments. *Acc. Chem. Res.* **2019**, *52*, 1575–1587. [CrossRef] [PubMed]
48. Zhang, Z.; Zhang, Q. Recent Progress in Well-Defined Higher Azaacenes (n ≥ 6): Synthesis, Molecular Packing, and Applications. *Mater. Chem. Front.* **2020**, *4*, 3419–3432. [CrossRef]
49. Ganschow, M.; Koser, S.; Hodecker, M.; Rominger, F.; Freudenberg, J.; Dreuw, A.; Bunz, U.H.F. Azaacenes Bearing Five-Membered Rings. *Chem. A Eur. J.* **2018**, *24*, 13667–13675. [CrossRef]
50. Cortizo-Lacalle, D.; Mora-Fuentes, J.P.; Strutyński, K.; Saeki, A.; Melle-Franco, M.; Mateo-Alonso, A. Monodisperse N-Doped Graphene Nanoribbons Reaching 7.7 Nanometers in Length. *Angew. Chem. Int. Ed.* **2018**, *57*, 703–708. [CrossRef] [PubMed]
51. Dolomanov, O.V.; Bourhis, L.J.; Gildea, R.J.; Howard, J.A.K.; Puschmann, H. OLEX2: A Complete Structure Solution, Refinement and Analysis Program. *J. Appl. Crystallogr.* **2009**, *42*, 339–341. [CrossRef]

52. Hafner, K.; Weldes, H. Zur Kenntnis Der Azulene II. Die Substitution Von Azulenen Mit Metallorganischen Verbindungen. *Justus Liebigs Ann. Chem.* **1957**, *606*, 90–99. [CrossRef]
53. Hatakenaka, R.; Nishikawa, N.; Mikata, Y.; Aoyama, H.; Yamashita, K.; Shiota, Y.; Yoshizawa, K.; Kawasaki, Y.; Tomooka, K.; Kamijo, S.; et al. Efficient Synthesis and Structural Analysis of Chiral 4,4′-Biazulene. *Chem. A Eur. J.* **2024**, *30*, e202400098. [CrossRef]
54. Karami, B.; Rooydel, R.; Khodabakhshi, S. A Rapid Synthesis of Some 1,4-Aryldiazines by the Use of Lithium Chloride as an Effective Catalyst. *Acta Chim. Slov.* **2012**, *59*, 183–188.
55. McDonald, R.N.; Wolfe, N.L.; Petty, H.E. Nonbenzenoid Aromatic Systems. VIII. Buffered Acetolysis of 2-(4- and 2-(6-Azulyl)Ethyl Arenesulfonates and 3-(4-Azulyl)-1-Propyl Nosylate. Examples of Ar3-5 and Ar3-6 Mechanisms. *J. Org. Chem.* **1973**, *38*, 1106–1113. [CrossRef]
56. Shuler, W.G.; Parvathaneni, S.P.; Rodriguez, J.B.; Lewis, T.N.; Berges, A.J.; Bardeen, C.J.; Krische, M.J. Synthesis and Photophysical Properties of Soluble N-Doped Rubicenes via Ruthenium-Catalyzed Transfer Hydrogenative Benzannulation. *Chem. A Eur. J.* **2021**, *27*, 4898–4902. [CrossRef]
57. Dittrich, B.; Fabbiani, F.P.A.; Henn, J.; Schmidt, M.U.; Macchi, P.; Meindl, K.; Spackman, M.A. Azulene Revisited: Solid-State Structure, Invariom Modeling and Lattice-Energy Minimization of a Classical Example of Disorder. *Acta Crystallogr. Sect. B* **2018**, *74*, 416–426. [CrossRef]
58. Rajnikant; Dinesh; Deshmukh, M.B.; Jadhav, S.; Kanwal, P. 2,3-Diphenylquinoxaline. *Acta Crystallogr. Sect. E Struct. Rep. Online* **2006**, *62*, o2356–o2357. [CrossRef]
59. Shoji, T.; Yamazaki, A.; Katoh, R.; Shimamura, K.; Sakai, R.; Yasunami, M.; Okujima, T.; Ito, S. Synthesis, Reactivity, and Properties of Benz[*a*]Azulenes via the [8+2] Cycloaddition of 2*H*-Cyclohepta[*b*]Furan-2-Ones with an Enamine. *J. Org. Chem.* **2022**, *87*, 5827–5845. [CrossRef]
60. Guo, J.; Du, F.; Yu, B.; Du, P.; Li, H.; Zhang, J.; Xin, H. Heptacyclic Aromatic Hydrocarbon Isomers with Two Azulene Units Fused. *Chem. Sci.* **2024**, *15*, 12589–12597. [CrossRef]
61. Xin, H.; Li, J.; Lu, R.; Gao, X.; Swager, T.M. Azulene–Pyridine-Fused Heteroaromatics. *J. Am. Chem. Soc.* **2020**, *142*, 13598–13605. [CrossRef]
62. Vardanyan, A.; Villinger, A.; Ehlers, P.; Langer, P. Synthesis and Properties of Carbo- and Heterocyclic Benz[a]Azulenes. *J. Org. Chem.* **2023**, *88*, 11411–11423. [CrossRef]
63. Bunting, J.W.; Meathrel, W.G. Quaternary Nitrogen Heterocycles. I. Equilibrium and Spectral Data for Pseudobase Formation by the N -Methyl Cations of Diazanaphthalenes. *Can. J. Chem.* **1972**, *50*, 917–931. [CrossRef]
64. Herges, R.; Geuenich, D. Delocalization of Electrons in Molecules. *J. Phys. Chem. A* **2001**, *105*, 3214–3220. [CrossRef]
65. Geuenich, D.; Hess, K.; Köhler, F.; Herges, R. Anisotropy of the Induced Current Density (ACID), a General Method to Quantify and Visualize Electronic Delocalization. *Chem. Rev.* **2005**, *105*, 3758–3772. [CrossRef]
66. Frisch, M.J.; Trucks, G.W.; Schlegel, H.B.; Scuseria, G.E.; Robb, M.A.; Cheeseman, J.R.; Scalmani, G.; Barone, V.; Petersson, G.A.; Nakatsuji, H.; et al. *Gaussian 16, Revision C.01*; Gaussian, Inc.: Wallingford, CT, USA, 2016.